Topotactic Growth of Edge-Terminated MoS2 from MoO2 Nanocrystals

Dahl-Petersen, Christian; Sari, Manuel; Brorson, Michael; Moses, Poul Georg; Rossmeisl, Jan; Lauritsen, Jeppe Vang; Helveg, Stig

Published in:
A C S Nano

Link to article, DOI:
10.1021/acsnano.8b00125

Publication date:
2018

Document Version
Peer reviewed version

Article

Topotactic Growth of Edge-Terminated MoS from MoO Nanocrystals

Christian Dahl-Petersen, Manuel Sari#, Michael Brorson, Poul Georg Moses, Jan Rossmeisl, Jeppe V. Lauritsen, and Stig Helveg

ACS Nano, **Just Accepted Manuscript** • DOI: 10.1021/acsnano.8b00125 • Publication Date (Web): 16 May 2018

Topotactic Growth of Edge-Terminated MoS_2 from MoO_2 Nanocrystals

Christian Dahl-Petersen[1,2], Manuel Sarić[3], Michael Brorson[1], Poul Georg Moses[1], Jan Rossmeisl[4], Jeppe Vang Lauritsen[2], Stig Helveg[1,*]

[1] Haldor Topsoe A/S, Haldor Topsøes Allé 1, DK-2800 Kgs. Lyngby, Denmark

[2] Interdisciplinary Nanoscience Center (iNANO), Aarhus University, Gustav Wieds Vej 14, DK-8000 Aarhus C, Denmark

[3] Technical University of Denmark, Department of Physics, DK-2800 Kgs. Lyngby, Denmark

[4] University of Copenhagen, Nano-Science Center, Department of Chemistry, Universitetsparken 5, DK-2100 Copenhagen, Denmark

*Address correspondence to sth@topsoe.com

Keywords. Topotaxy, growth mechanism, MoS_2, edge-termination, *in situ* transmission electron microscopy, density functional theory

Abstract.

Layered transition metal dichalcogenides have distinct physicochemical properties at their edge-terminations. The production of an abundant density of edge structures is, however, impeded by

the excess surface energy of edges compared to basal planes and would benefit from insight into the atomic growth mechanisms. Here, we show that edge-terminated MoS_2 nanostructures can form during sulfidation of MoO_2 nanocrystals by using *in situ* transmission electron microscopy (TEM). Time-resolved TEM image series reveal that the MoO_2 surface can sulfide by inward progression of MoO_2(20-2):MoS_2(002) interfaces resulting in upright-oriented and edge-exposing MoS_2 sheets. This topotactic growth is rationalized in interplay with density functional theory calculations by successive O-S exchange and Mo sublattice restructuring steps. The analysis shows that *e*-MoS_2 formation is energetically favorable at MoO_2(110) surfaces and provides a necessary requirement for the propensity of a specific MoO_2 surface termination to form edge-terminated MoS_2. Thus, the present findings should benefit the rational development of transition metal dichalcogenide nanomaterials with abundant edge-terminations.

Progress in the synthesis of layered transition metal dichalcogenides (TMDCs) has led to a variety of nanoscale structures including fullerenes, tubes/wires and platelets, each with distinct physicochemical properties.[1] These TMDC structures are derived from layers of hexagonally arranged transition metal atoms (*e.g.* Mo and W) in which each metal atom is coordinated by six chalcogenide atoms usually in a trigonal prismatic geometry. Such TMDC sheets are terminated by extended basal planes with a regular atomic arrangement and by atomically thin edges. Due to the reduced atomic coordination, the edges expose structures that markedly differ from those of the basal plane and, in turn, offer distinct electronic,[2,3] optical,[4] magnetic[5] and chemical[6,7] properties. In particular, the edges of MoS_2 sheets have long received interest as catalysts for mineral oil refining,[8,9] hydrogen evolution,[10,11] CO_2 reduction[12] and photo-oxidation[13] reactions, whereas the unperturbed MoS_2 basal plane is regarded as essentially inert. These catalytic

processes would therefore benefit from edges that are more abundantly available. In addition, exposed edges are also beneficial for reducing steric hindrance in adsorption of *e.g.* heavy sulfur-containing organic compounds, which is a prime target in improving catalysts for oil refining processes.[14]

The availability of edge sites depends on the size, shape and orientation of the TMDC sheets. As the edge terminations are associated with a considerably higher surface energy than the basal plane, the formation of edge sites is suppressed compared to the growth of basal planes. Hence, TMDC sheets are expected to form with extended basal plane exposed to the surroundings and oriented parallel with a supporting surface. In contrast, the sulfidation or thermolysis of molybdenum precursors dispersed on a support material have empirically been found to also produce upright-oriented and thereby edge-exposing MoS_2 sheets.[12,13,15-26] Common for the majority of these edge-favoring synthesis procedures is the employment of a dense molybdenum precursor in the form of nanoparticles or thin films.[12,13,15,18-23] The appearance of the upright orientation has been attributed to a strong bonding of the MoS_2 edge to the supporting material to counteract the thermodynamic drive towards a parallel orientation.[16,27,28] However, an elaborate understanding of the atomic mechanisms governing the formation of the edge-terminated MoS_2 is still lacking and bottom-up strategies have therefore not been available for synthesizing edge-terminated materials with superior catalytic and other functionalities.

With recent advances in transmission electron microscopy (TEM), dynamic transformations of solid materials can now be monitored *in situ* at high spatial resolution during exposure to reactive gas or liquid environments. By acquiring time-lapsed series of TEM images, it has become possible to gain insight into the mechanisms and kinetics involved in the formation

of different types of nanometer-sized structures.[29-31] Here, we employ this TEM approach to monitor the growth of MoS_2 nanostructures from molybdenum(IV) oxide (MoO_2) nanocrystals *in situ* during exposure to a reactive H_2S/H_2 atmosphere. The time-resolved TEM image series reveal that the oxide nanocrystal surfaces can form domains of upright-oriented MoS_2 sheets by the progression of the MoO_2(20-2):MoS_2(002) interface from the MoO_2 surface toward its bulk, in addition to domains of parallel-oriented MoS_2 sheets (Figure 1a). This topotactical reaction is explained in interplay with density functional theory (DFT) modelling by repeated steps of O-S exchange and Mo sublattice restructuring. Specifically, these reaction steps exhibit a marked dependency of the MoO_2 surface structure in the way that energetically favors formation of edge-terminated MoS_2 sheets at the MoO_2(110) surface. The implication of these findings is therefore that (110)-terminated MoO_2 precursors can produce abundantly available MoS_2 edge sites and that the reaction steps offer descriptors for surface topotaxy, which should, in general, facilitate the design of TMDC nanomaterials with superior edge functionalities.

Results/Discussion

The electron microscope experiments used MoO_2 nanoparticles as precursor because (1) previous studies suggested that molybdenum-dense precursors favor formation of upright-oriented MoS_2 sheets, (2) nanoparticles enable surface-profile imaging by electron microscopy and (3) reduced MoO_3, such as MoO_2 and MoO_{3-x}, has been considered as intermediate in sulfidation by H_2S/H_2 into inorganic fullerene structures.[32,33] The molybdenum(IV) oxide precursor was formed by heating ammonium heptamolybdate tetrahydrate ($(NH_4)_6[Mo_7O_{24}]\cdot 4H_2O$) to 450°C at the base vacuum of ca. $5x10^{-6}$ mbar (Methods). The procedure resulted in nanoparticles with projected diameters in the range of 5 to 20 nm and with

the monoclinic MoO_2 crystal structure[34,35] (Figures S1 and S2 in the Supporting Information). The MoO_2 nanocrystals exposed predominantly low-indexed facets such as *e.g.* (100), (010) and (110) (Figure S2 in the Supporting Information). Subsequently, the as-prepared MoO_2 nanocrystals were exposed to a gas mixture of 10% H_2S in H_2 at a total pressure of 1 mbar and heated to a nominal temperature of 250-300°C for 240-300 min inside the electron microscope (Methods). Such low temperatures have previously been associated with the synthesis of upright-oriented MoS_2 sheets.[16,17] During the present treatment, structures emerged that are attributed to molybdenum sulfide because they were absent in similar experiments without H_2S in the reaction gas (Figure S3 in the Supporting Information). The molybdenum sulfide structures appeared with two distinctly different orientations relative to the surface of the MoO_2 nanocrystals.

The first structure, denoted *e*-MoS_2, represents our main finding and surprisingly consists of sheets oriented upright with respect to the projected nanocrystal surface (Figure 1a). The sheets represent lattice fringes with spacing of ca. 0.62 nm, corresponding to the MoS_2 (002) lattice planes (Figure 1b). Domains of *e*-MoS_2 extend from the projected periphery towards the bulk of the nanocrystal and typically consist of 3-8 MoS_2 sheets with length of 1 - 5 nm (Figure 1b and Figures S4-S6 in the Supporting Information). Thus, *e*-MoS_2 exposes predominantly edge sites to the surroundings. Due to the projection geometry, it is possible that the *e*-MoS_2 only partly covers the corresponding surface termination oriented along the electron beam direction (Figure 2) and that the remaining MoO_x sites eventually sulfide to cover the nanocrystal surface by *p*-MoS_2. Moreover, the anisotropy of MoS_2 sheets implies that the corresponding TEM image contrast depends strongly on their orientation. MoS_2 sheets oriented with their (002) basal plane along the electron beam direction obtain strong phase contrast in high-resolution TEM images, whereas MoS_2 sheets having the (002) planes tilted more than ca. 9° off the electron beam

direction appear with a markedly diminished contrast due to the reduced number of atoms contributing to the projected electrostatic potential.[36,37] Therefore, domains of *e*-MoS_2 may be present in other parts of the MoO_2 nanocrystal and remain unresolved in the TEM images due to their orientation. It is therefore not surprising that the *e*-MoS_2 structure was observed in only about 13% of all nanocrystals (Note in the Supporting Information). However, the low abundance of *e*-MoS_2 could also reflect that only certain surface facets of the parent MoO_2 nanocrystal promote growth of the edge-terminated MoS_2.

The second structure, denoted *p*-MoS_2, consists of sheets contouring the surface of most of the MoO_2 nanocrystals (Figure 1a, note in the Supporting Information). Occasionally, these sheets stack with an interlayer spacing of ca. 0.63 nm, corresponding to the MoS_2(002) lattice planes, and reveal internal lattice fringes with spacing of 0.27 nm, corresponding to (100) lattice planes (Figure 1b and 1c). The *p*-MoS_2 sheets extend along the projected MoO_2 surface parallel to the electron beam. In addition, the sheets are likely also contouring those parts of the MoO_2 nanocrystal surface that is *not* parallel with the electron beam direction (within $\sim\pm9^{o}$) and *p*-MoS_2 therefore remain undetectable in such regions of the TEM images due to their orientation and overlaid contrast from the projected bulk MoO_2 nanocrystal. Thus, the *p*-MoS_2 structure consists of MoS_2 sheets that are confined to the surface region of the MoO_2 nanocrystal and expose predominantly the MoS_2(002) basal plane, similarly to previous findings for fullerene MoS_2 structures.[32,33,38]

To address the growth mode of the edge-terminated MoS_2, *e*-MoS_2, an analysis is first presented of time-resolved series of TEM images that were acquired of individual MoO_2 nanocrystals as the sulfidation reaction progressed. Figure 2 shows an image sequence (extracted from Video S1 in the Supporting Information) revealing the dynamic transformation of the

surface on a MoO_2 nanocrystal during sulfidation. The images show that the MoS_2 sheets nucleate directly in the exposed MoO_2 surface without any additional surface layers. Adjacent MoS_2 sheets form simultaneously and establish a domain of *e*-MoS_2. Subsequently, the MoS_2 sheets grow in length from the original surface toward the bulk of the MoO_2 nanocrystal, reaching a final length of ca. 2.8 nm. Figure S7 in the Supporting Information shows that the MoS_2 sheets grow initially fast and that the growth stagnates at longer sulfidation times. The decay of the growth rate may be due to the slower mass transport through the bulk of the nanoparticle. Similar dynamic behavior is revealed in the formation of shorter *e*-MoS_2 structures albeit at a corresponding lower signal-to-noise ratio (Figure S5 in the Supporting Information). On average, *e*-MoS_2 sheets observed *in situ* grew to a final average projected length of 1.7 nm (with a standard deviation of 0.6 nm) and sheets observed *post mortem* had grown to an average projected length of 1.8 nm (with a standard deviation of 0.7 nm) (Figure S8 in the Supporting Information). This conformity demonstrates that alterations of the growth process induced by the electron illumination were insignificant with the applied low dose-rate imaging protocol and that the observed MoS_2 formation is inherent to the sulfidation reaction as such (Methods). Thus, the time-resolved observations indicate that growth of *e*-MoS_2 proceeded by an O-S exchange reaction and by an inward progression of the MoO_2:MoS_2 interface from the surface of the MoO_2 nanocrystal upon continued exposure to the sulfur-rich gas.

To address the relation between the *e*-MoS_2 and MoO_2 host nanocrystal structures, their interface is examined at the atomic-scale. Figure 3 shows a close-up TEM image of the interface, which reveals a threefold periodicity with three MoO_2(20-2) lattice planes matching one single MoS_2(002) lattice plane. The lattice matching at the interface influenced the MoS_2 interlayer spacing in such a way that the spacing varied with the distance from the MoO_2:MoS_2 interface to

the nanocrystal surface. Specifically, the MoS_2(002) lattice spacing was larger closer to the interface, corresponding to $3a_{MoO2[20-2]}$ = 0.73 nm, and smaller near the nanocrystal surface, corresponding to $a_{MoS2[002]}$ = 0.62 nm (Figure 3). Consistently, shorter *e*-MoS_2 slabs were separated by ca. 0.73 nm (Figures S4 and S6 in the Supporting Information). The larger MoS_2(002) lattice spacing near the interface constitutes a geometric strain of +17%, which is energetically feasible due to the weak van der Waals interaction between the MoS_2 sheets. A similar analysis of the crystal lattice planes in high-resolution TEM images of nine additional MoO_2 nanocrystals also characterized the interface as MoO_2(20-2):MoS_2(002) (Figure S4 in the Supporting Information). This interfacial relation of the two crystal lattices shows that the *e*-MoS_2 sheets formed as the result of a topotactic transformation of the MoO_2 surface region.[39] Moreover, as the MoS_2 sheets are oriented upright with respect to the projected MoO_2 surface, *e*-MoS_2 must nucleate at surface facets inclined from the MoO_2(20-2) lattice planes, including the more abundant low-indexed surface terminations, such as (110), (010) and (100).

Furthermore, the conversion of MoO_2 into MoS_2 by anion exchange also entails a restructuring of the Mo sublattice due to different Mo atom densities. MoO_2 is a monoclinic structure with a density of 30.4 Mo atoms/nm^3, and MoS_2 is a hexagonal structure with a density of 18.8 Mo atoms/nm^3. The corresponding volume expansion of 62% per Mo atom implies that Mo atoms were expelled from the bulk MoO_2 during formation of *e*-MoS_2. These Mo atoms possibly contributed to *p*-MoS_2, because *p*-MoS_2 and *e*-MoS_2 formed simultaneously (Figure 2) and *p*-MoS_2 formed at the exterior surface of the MoO_2 nanocrystals, causing an apparent increase in the projected size of the nanocrystals (Figure S9 in the Supporting Information).

The present observations of topotactic growth of edge-terminated MoS_2 sheets from MoO_2 can be rationalized by the atomistic mechanism proposed in Figure 4. The consistency of

this mechanism is examined by means of DFT calculations, combined with a thermodynamic extrapolation to the present sulfidation conditions (Methods). First, the conversion of bulk MoO_2 to MoS_2 is addressed by the reaction:

$$MoO_2\ (s) + 2\ H_2S\ (g) \rightarrow MoS_2\ (s) + 2H_2O\ (g) \quad (1)$$

For this reaction, a calculation shows a Gibbs free energy change of -1.00 eV, corresponding to an average gain of -0.50 eV/S atom, with 0.9 mbar H_2 and 0.1 mbar H_2S at 250 ^oC. The sulfidation described by eq. (1) initiates at the MoO_2 surface.[40,41] The surface sulfidation by H_2S is modelled at the low-indexed (110), (010) or (100) facets of MoO_2, consistent with the TEM observations. This process is associated with a free energy change of -0.01 eV/S atom, -0.29 eV/S atom and +0.09 eV/S atom for the MoO_2 (110), (010) and (100) surfaces, respectively, at the same conditions. Thus, only the (110) and (010) surface terminations tend to sulfide (Figure S10 in the Supporting Information), whereas the (100) surface remains oxidic under the present reaction conditions.

Following the initial sulfidation, the MoO_2 surface is envisioned to develop by successive steps of Mo sublattice reconstruction and O-S exchange to accommodate the upright oriented MoS_2 sheets. At the sulfided MoO_2(110) surface, every second topmost [-11-1]-row contains half the number of Mo atoms (row 1 and 3 in Figure 4a) compared to the [-11-1]-rows in the bulk MoO_2 structure (row 4 and 5 in Figure 4a). A stepwise displacement of these topmost [-11-1]-rows toward each other, by $1a_{[20-2]}$ as outlined for row 1 (a → b in Figure 4) and row 3 (b → c in Figure 4), results in a sulfided row of Mo atoms with a density similar to MoS_2[100] (note in the Supporting Information). Moreover, the repetition of the displacements along the MoO_2 surface develops a threefold periodicity of MoO_2(20-2):MoS_2(002) interface, in agreement with the TEM images. The [-11-1]-row displacements uncover underlying oxide [-11-1]-rows (row 2, 4 and 5

in Figure 4) comparable to the pristine oxide surface. As the exposure to the sulfiding environment is continuous in the experiments, these oxide rows likewise undergo O-S exchange as well. A two-row high MoS_2 sheet therefore emerges extending one row in and out from the initial surface (row 1+3 and 2 in Figure 4c). Moreover, the deeper-lying MoO_2 [-11-1]-rows also partly sulfide upon exposure to the reaction environment (row 4 and 5), and these rows may subsequently transform in a similar way as the outermost rows (row 1 and 3). That is, half of the sulfided Mo atoms in the [-11-1]-rows (row 4 and 5) are displaced into an additional sheet that extends the *e*-MoS_2 sheet outwards. The remaining half-filled Mo [-11-1]-rows (row 4 and 5) mimic the initial state of the sulfided surface (Figure 4a) and therefore undergo the same transformations, resulting in a four-row *e*-MoS_2 sheet (Figure 4d). As a result, the mechanism outlined in Figure 4 a-d becomes cyclic and, in turn, develops an *e*-MoS_2 structure with a MoO_2(20-2):MoS_2(002) interface and a threefold periodicity, consistent with the experimental observations. To corroborate this mechanism, the O-S exchange and Mo [-11-1]-row displacement steps were examined by DFT calculations to evaluate the Gibbs free energy for each state (Methods). Figure 4e shows a successive lowering of the Gibbs free energy per unit cell as the sulfidation reaction progressed, demonstrating that the proposed mechanism for the topotactic growth of *e*-MoS_2 at the MoO_2(110) surface is plausible.

The mechanism in Figure 4 implies that the *e*-MoS_2 sheets grow to the same extent inward and outward from the original MoO_2 surface. In contrast, the MoS_2 sheets are observed to progress mainly inward and only modestly outward from the original MoO_2 surface in the experiment (Figure 2). The asymmetric growth of the *e*-MoS_2 sheets possibly occurs under the experimental conditions, because the Mo atoms expelled from the MoO_2 bulk are free to migrate to sites on the MoO_2 surface where incorporation into *p*-MoS_2 can occur. In contrast, in the DFT

modelling the same Mo atoms are added as an outward extension of the MoS_2 layer, due to the geometrical constraint of the employed unit cell. The difference may reflect that, in the experimental situation, the outward growth is kinetically limited or the emergence of the basal plane of *p*-MoS_2 is energetically favored over *e*-MoS_2 sheets protruding outward from the original the MoO_2 surface.

To address the surface dependency of the topotactic reaction, the sulfidation mechanism is compared on the MoO_2 (110) and (010) surfaces (Figure 4 and Figure S11 in the Supporting Information). For both surfaces, the energy gain upon sulfidation is lower than the limit set by equation (1) for growth of bulk MoS_2 from MoO_2 (0.50 eV/S atom). Specifically, for the MoO_2 (110) and (010) surface, the corresponding Gibbs free energy difference from the surface to bulk sulfidation is -0.49 eV/S-atom (-0.50 eV/S atom minus -0.01 eV/S atom) and -0.21 eV/S atom (-0.50 eV/S atom minus -0.29 eV/S atom), respectively, under the present conditions. Thus, S atoms are less stable on the (110) than the (010) surface with respect to the *e*-MoS_2 structure. In addition, the Mo sublattice restructuring also exhibits a surface-dependency. Whereas displacement of the [-11-1] rows is spontaneous on the MoO_2(110) surface (a → b in Figure 4e), the displacement of [101]-rows on the MoO_2(010) surface into a one-row high MoS_2 sheet (a → b in Figure S11 in the Supporting Information) is associated with a Gibbs free energy change of +2.74 eV/unit-cell (Figure 4e). This energy change results from the higher Mo atom density in the (010) surface (note in the Supporting Information) and adds a barrier for restructuring the Mo sublattice that suppresses growth of *e*-MoS_2. Thus, the calculations show that growth of *e*-MoS_2 is favored on MoO_2(110) due to the large energy gain for transferring surface S atoms into bulk MoS_2 and the spontaneous and facile restructuring the Mo sublattice, whereas formation of *e*-

MoS_2 is hindered on MoO_2(010) due to the smaller energy gain in the S transfer and the larger barrier for Mo sublattice restructuring.

Conclusion

The present study demonstrates the O-S exchange energy and the Mo sublattice reconstruction energy as descriptors for the propensity of a specific MoO_2 surface to form *e*-MoS_2, and the analysis provides a necessary requirement for a MoO_2 surface to facilitate a spontaneous topotactic transformation into edge-terminated MoS_2. This insight may help understanding previous reports on oriented nucleation and growth of MoS_2 sheets based on the surface properties of the molybdenum oxide precursors.[16-18] Moreover, the present findings suggest that the *e*-MoS_2 growth is energetically favored at (110) surfaces of a MoO_2 nanomaterials under the present growth conditions. In the future, developing shape-selective synthesis procedures of MoO_2 nanomaterials with an enhanced abundance of (110) surface terminations therefore seems as one viable route for optimizing the abundance of *e*-MoS_2. The *e*-MoS_2 formation could be kinetically limited by adsorption or diffusion processes not considered in the present analysis. Such limitations can be addressed by detailed characterization using oxygen adsorption of the MoS_2 edge sites[42] and a shape-determination of the MoO_2 nanomaterial using electron microscopy or X-ray diffraction.[43] Conceptually, the present descriptors of surface topotaxy may be generally applicable in guiding bottom-up synthesis procedures of TMDC nanomaterials towards enhanced edge-functionalities.

Methods/Experimental

Sample preparation and sulfidation. Ammonium heptamolybdate tetrahydrate, $(NH_4)_6Mo_7O_{24}\cdot 4H_2O$ (Merck, 1180336, minimum 99% nominal purity) was used as molybdenum precursor. The precursor granulate was ground to a fine powder and dispersed in its dry state onto plasma-cleaned Protochips Aduro E-chips or FEI Company NanoEx chips. Precursor particles were approximately 2-5 μm wide and overhung the membrane holes near the center of the chip membrane. Heating of the chips to 450°C in the microscope base vacuum transformed the precursor into MoO_2 nanoparticles ranging from 5 to 20 nm in width. For the Aduro E-chips, MoO_2 nanoparticles protruding from holes in the second innermost quadrant of 7x7 hole arrangement were examined in the electron microscope to ensure temperature uniformity[44] and to minimize the image contrast contribution from the chip membranes. The NanoEx chips have a uniform temperature across the perforated membrane,[45] and particles protruding from any hole were imaged by TEM.

To initiate the sulfidation reaction, the temperature of the chip was lowered to 300°C or 250°C, and subsequently a premixed gas with 10% H_2S in H_2 (Air Liquide, nominal purity 98% for H_2S and 99.999% for H_2) was introduced into the electron microscope at time = 0 min. The gas composition was continuously monitored using a quadrupole mass spectrometer (Balzers Prisma QMS 200) positioned at the microscope second differential pumping step for masses 2, 16, 18, 32, 33 and 34 AMU corresponding to signals from H_2, O_2, H_2O, S, HS, and H_2S. This showed that a constant gas composition was obtained after 5 min at constant gas pressure (Figure S12 in the Supporting Information). The ion currents were sampled at a total acquisition time of 11 sec.

Transmission electron microscopy (TEM). The growth of MoS_2 was examined by means of a Philips CM300 FEG-ST transmission electron microscope, which is equipped with a differential pumping system and heating stages to enable the exposure of solid specimens to reactive gasses and elevated temperatures.[37,46] Specifically, this microscope is dedicated to experiments including corrosive sulfur-containing gases.[37] The microscope was operated at a primary electron energy of 300 keV and with an electron dose-rate of 150 $e^-/(Å^2s)$ for *in situ* observations with 10% H_2S in H_2 at 1 mbar total pressure in the sample region and of 200 $e^-/(Å^2s)$ for *post mortem* observations under a high vacuum of better than $5x10^{-6}$ mbar in the sample region. The applied gas environment reduced the electron transmittance by only ca. 3% relative to vacuum. Therefore, electron doses and dose-rates are quoted with reference to measurements in the evacuated microscope. Moreover, the microscope projection system was set at a magnification corresponding to an effective pixel size ranging from 0.03 nm to 0.07 nm of the charged coupled device (CCD) camera (Tietz F114) during TEM image acquisition. These magnification settings are sufficient to resolve the MoS_2 (100) lattice planes of spacing 0.27 nm and the MoO_2 (20-2) lattice planes of spacing 0.24 nm, as the shortest lattice spacings. Moreover, imaging was done at focus settings close to the Scherzer defocus value of f = -64 nm to ensure a large contrast information transfer for the MoS_2 (002) and (100) lattice planes and the MoO_2 (20-2) lattice planes. The CCD illumination time was 0.5 - 1 s per image.

The experiments were conducted using micro-electro-mechanical heaters as sample support. A part of the experiments employed the Protochips Aduro system, which consists of silicon chips supporting silicon carbide membranes perforated with 7x7 holes near the center.[47] Prior to sample loading, chips were exposed to Ar/O_2 plasma for cleaning. In the experiment, sample dispersed on the membranes was heated by resistively passing an electrical current

through the membrane. The membrane current-temperature characteristic was calibrated using pyrometry at a pressure of $1.3x10^{-2}$ mbar by the manufacturer (Protochips). During gas exposure in the microscope, additional heat dissipation to the gas phase was accounted for by operating the membrane in a constant resistance mode.[37] The other part of the experiments employed the FEI Company NanoEx system, which consists of silicon chips with a silicon nitride membrane perforated with 22 holes near its center and a conductive thin film with four electrodes for resistive heating and on-board temperature sensing.[45] Prior to sample loading, chips were also exposed to Ar/O_2 plasma for cleaning. The temperature-resistance characteristic of the chips was provided by the manufacturer (FEI Company).

During a sulfidation experiment, 3-4 sample regions were monitored. The regions were located at distances larger than the width of the electron beam, so that the regions were monitored separately. As sulfidation of the sample progressed, each region was imaged every approximately 15 min. and each imaging step lasted for a maximum of 60 s for positioning, focusing and image acquisition. The total experiment duration was 240-300 min, corresponding to a total of up to 21 electron beam exposures of each region. The maximal total accumulated electron dose incident on a region in the *in situ* experiments was therefore $189x10^3$ $e^-/Å^2$, using an electron dose rate of 150 $e^-/(Å^2s)$. At each position and time step, an image series of 5 or 10 sequential images was acquired. These images were post-aligned using cross-correlation and summed to the final displayed images with improved signal-to-noise-ratio. Immediately after an imaging step, the electron beam was moved to the next sample position. This imaging strategy was applied to minimize the total dose rate while maintaining a detectable image signal.[48] Additional images series were obtained after termination of the sulfidation reaction at positions

without prior exposure to the electron beam (*post mortem*). These *post mortem* images were acquired at a base vacuum below $5x10^{-6}$ mbar and 120°C.

The magnification of the TEM images was calibrated relative to a standard Au/C calibration grid. The images are represented as a direct representation of the summed CCD current outputs in a monochromatic green color scale with only a linear adjustment of the image contrast and brightness.

Image simulation. High-resolution TEM images of MoO_2 were simulated using the multi-slice approach as implemented in the MacTempasX software.[49] To describe the Philips CM300 microscope, the simulations employed an incident electron beam energy of 300 keV, spherical aberration coefficient of C_s = 1.4 mm, a convergence angle of 0.3 mrad, a defocus spread of 8.3 nm, an outer objective aperture of 0.14 nm, and a mechanical vibration amplitude in the imaging plane of 0.07 nm. The MoO_2 nanoparticles were described by a monoclinic MoO_2 crystal structure[32] belonging to the $P2_1/c$ space group.

Theoretical calculations. The GPAW[50,51] density functional theory code was employed in finite difference mode using a grid spacing of 0.18 Å to obtain total energies. The exchange and correlation was described by the revised Perdew-Burke-Ernzerhof (RPBE) functional. All atomic positions in the systems involving MoO_2 and MoS_2 structures were relaxed until the largest interatomic force was smaller than or equal to 0.05 eV/Å and the molecules were relaxed to a value less than 0.01 eV/Å. The DFT electronic energies of H_2S and H_2O were corrected with zero-point energies and entropic contributions. The zero-point energy corrections were obtained by performing vibrational analysis calculations in GPAW using the harmonic approximation.[52] The remaining thermodynamic corrections were obtained from thermochemical tables.[53] The calculations employed reaction conditions at 250°C with 0.1 mbar H_2S and 0.9 mbar H_2,

matching the experimental sulfidation conditions. The calculations used an estimated H_2O pressure of 10^{-3} mbar to reflect an upper limit of the residual gas phase in the electron microscope.

The bulk structure of monoclinic MoO_2 was modeled using a unit cell consisting of 4 Mo and 8 O atoms periodic in the x, y and z directions, respectively. Bulk MoS_2 was modeled as infinite layers periodic in the x [110] and y [1-10] directions, separated by vacuum in the z [002] direction and with 2 Mo and 4 S atoms in the unit cell. The Brillouin zone was sampled with 8,8,8 k-points in the x, y and z directions, respectively, both for bulk MoO_2 and MoS_2. The surfaces were modeled as symmetric layers of six (010) or (110) MoO_2 layers periodic in the x [20-2] and y [101] or [-11-1] lattice directions and separated by 13 Å of vacuum in the z [010] or [110] direction to prevent the surfaces from interacting due to the periodic boundary conditions. The DFT calculations of the MoO_2 surface employed a periodicity of 4 along the [20-2] direction. Importantly, the unit cell dimension of 4x $a_{[20-2]}$ is longer than the observed periodicity of 3x $a_{[20-2]}$ at the MoO_2:MoS_2 interface (Figure 3). The longer periodicity employed in the DFT calculations ensured that periodic boundaries could be invoked and kept the computational time low. Moreover, the periodicity in the DFT calculations is a pure geometric effect, because identical exchange and Mo sublattice restructuring occurs locally in the larger cell and the extra surface energy is canceled out by the reference (Figure 4a). Therefore, the present calculations still capture the energetics in the transformation of three MoO_2 planes into one MoS_2 sheet.

The Brillouin zone of the MoO_2 for the (010) and (110) surface slabs were sampled with 4, 4, 1 k-points in the x [20-2], y [101] or [-11-1] and z [010] or [110] directions, respectively. The energies for the surface sulfidation were obtained by replacing all directly gas exposed O atoms with S atoms and using gas phase H_2O and H_2S as references. For the calculations

regarding the reconstructive growth mechanism of MoS_2 the unit cell had to be repeated once in the x direction for the MoO_2 (010) and in the y direction for the MoO_2 (110) surface in order to prevent the formed MoS_2 sheets from overlapping. The Brillouin zone was thus sampled with 4, 2, 1 k-points for the (010) system and 2, 4, 1 k-points for the (110) system in the x [20-2], y [101] or [-11-1] and z [010] or [110] directions, respectively. Details regarding calculation of the data points in Figure 4e are given in Supplementary methods in the Supporting Information.

Acknowledgment.

The work was performed at the electron microscope facility at Haldor Topsoe A/S. CDP acknowledges financial support from Innovation Fund Denmark (grant Cat-C), and MS acknowledges financial support from Innovation Fund Denmark (grant HYDECAT). The authors acknowledge S. Ullmann (Haldor Topsoe A/S), S. Kegnæs (Technical University of Denmark (DTU)) and Q. Ramasse (SuperSTEM, UK) for fruitful discussions.

Supporting Information.

Note, Supplementary methods and Figures S1-S12 (PDF)

Video S1 accompanies Figure 2 and shows a MoO_2 nanocrystal during the exposure to 1 mbar of 10% H_2S in H_2 at 250°C. The images are recorded with 15 min intervals, with the first image equivalent to 45 min of gas exposure. The movie is displayed with 2 frames per second. Each frame corresponds to an image series of 5 exposures, which are post-aligned using cross-correlation and summed to improve the image signal-to-noise ratio. description (AVI)

References

1 Tenne, R. Inorganic Nanotubes and Fullerene-like Nanoparticles. *Nat. Nanotechnol.* **2006**, 1, 103-111.

2 Xu, H.; Liu, S.; Ding, Z.; Tan, S. J. R.; Yam, K. M.; Bao, Y.; Nai, C. T.; Ng, M.-F.; Lu, J.; Zhang, C Loh, K. P. Oscillating Edge States in One-Dimensional MoS_2 Nanowires. *Nat. Commun.* **2016**, 7, 12904.

3 Bollinger, M. V.; Lauritsen, J. V.; Jacobsen, K. W.; Nørskov, J. K.; Helveg, S.; Besenbacher, F. One-Dimensional Metallic Edge States in MoS_2. *Phys. Rev. Let.* **2001**, 87, 196803.

4 Yin, X.; Ye, Z.; Chenet, D. A.; Ye, Y.; O'Brien, K.; Hone, J. C.; Zhang, X. Edge Nonlinear Optics on a MoS_2 Atomic Monolayer. *Science* **2014**, 344, 488-490.

5 Vojvodic, A.; Hinnemann, B.; Nørskov, J. K. Magnetic Edge States in MoS_2 Characterized by Density-Functional Theory. *Phys. Rev. B* **2009**, 80, 125416.

6 Chhowalla, M.; Shin, H. S.; Eda, G.; Li, L.-J.; Loh, K. P.; Zhang, H. The Chemistry of Two-Dimensional Layered Transition Metal Dichalcogenide Nanosheets. *Nat. Chem.* **2013**, 5, 263-275.

7 Deng, D.; Novoselov, K. S.; Fu, Q.; Zheng, N.; Tian, Z.; Bao, X. Catalysis with Two-Dimensional Materials and their Heterostructures. *Nat. Nanotechnol.* **2016**, 11, 218-230.

8 Prins, R. Energy-Related Catalysis: Hydrotreating Reactions: Hydrodesulfurization, Hydrodenitrogenation, Hydrodeoxygenation and Hydrodechlorination in *Handbook of Heterogeneous Catalysis* (eds. Ertl, G., Knözinger, H. & Weitkamp, J.), Wiley-VCH Verlag GmbH, 2008.

9 Besenbacher, F.; Brorson, M.; Clausen, B.S.; Helveg, S.; Hinnemann, B.; Kibsgaard, J.; Lauritsen, J.V.; Moses, P.G.; Nørskov, J.K.; Topsøe, H. Recent STM, DFT and HAADF-STEM Studies of Sulfide-Based Hydrotreating Catalysts: Insight into Mechanistic, Structural and Particle Size Effects. *Catal. Today* **2008**, 130, 86-96.

10 Jaramillo, T.F.; Jørgensen, K.P.; Bonde, J.; Nielsen, J.H.; Horch, S.; Chorkendorff, I. dentification of Active Edge Sites for Electrochemical H_2 Evolution from MoS_2 Nanocatalysts. *Science* **2007**, 317, 100-102.

11 Hou, Y.; Abrams, B. L.; Vesborg, P. C. K.; Björketun, M. E.; Herbst, K.; Bech, L.; Setti, A. M.; Damsgaard, C. D.; Pedersen, T.; Hansen, O.; Rossmeisl, J.; Dahl, S.; Nørskov, J. K.; Chorkendorff, I. Bioinspired Molecular Co-Catalysts Bonded to a Silicon Photocathode for Solar Hydrogen Evolution. *Nat. Mater.* **2011**, 10, 434-438.

12 Asadi, M.; Kumar, B.; Behranginia, A.; Rosen, B. A.; Baskin, A.; Repnin, N.; Pisasale, D.; Phillips, P.; Zhu, W.; Haasch, R.; Klie, R. F.; Král, P.; Abiade, J.; Salehi-Khojin, A. Robust Carbon Dioxide Reduction on Molybdenum Disulphide Edges. *Nat Commun.* **2014**, 5, 4470.

13 Liu, C.; Kong, D.; Hsu, P.-C.; Yuan, H.; Lee, H.-W.; Liu, Y.; Wang, H.; Wang, S.; Yan, K.; Lin, D.; Maraccini, P. A.; Parker, K. M.; Boehm, A. B.; Cui, Y. Rapid Water Disinfection using Vertically Aligned MoS_2 Nanofilms and Visible Light. *Nat. Nanotechnol.* **2016**, 11, 1098-1104.

14 Tuxen, A. K.; Füchtbauer, H. G.; Temel, B.; Hinnemann, B.; Topsøe, H.; Knudsen, K. G.; Besenbacher, F.; Lauritsen, J. V. Atomic-Scale Insight into Adsorption of Sterically Hindered Dibenzothiophenes on MoS_2 and Co–Mo–S Hydrotreating Catalysts. *J. Catal.* **2012**, 295, 146-154.

15 Hayden, T. F.; Dumesic, J. A. Studies of the Structure of Molybdenum Oxide and Sulfide Supported on Thin Films of Alumina. *J. Catal.* **1987**, 103, 366-384.

16 Sakashita, Y.; Araki, Y.; Honna, K.; Shimada, H. Orientation and Morphology of Molybdenum Sulfide Catalysts Supported on Titania Particles, Observed by using High-Resolution Electron Microscopy. *Appl. Catal., A* **2000**, 197, 247-253.

17 Shimada, H. Morphology and Orientation of MoS_2 Clusters on Al_2O_3 and TiO_2 Supports and their Effect on Catalytic Performance. *Catal. Today* **2003**, 86, 17-29.

18 Kibsgaard, J.; Chen, Z. B.; Reinecke, B. N.; Jaramillo, T. F. Engineering the Surface Structure of MoS_2 to Preferentially Expose Active Edge Sites for Electrocatalysis. *Nat. Mater.* **2012**, 11, 963-969.

19 Kong, D.; Wang, H.; Cha, J. J.; Pasta, M.; Koski, K. J.; Yao, J.; Cui, Y. Synthesis of MoS_2 and $MoSe_2$ Films with Vertically Aligned Layers. *Nano Lett.* **2013**, 13, 1341-1347.

20 Wang, H.; Kong, D.; Johanes, P.; Cha, J. J.; Zheng, G.; Yan, K.; LiU, N.; Cui, Y. $MoSe_2$ and WSe_2 Nanofilms with Vertically Aligned Molecular Layers on Curved and Rough Surfaces. *Nano Lett.* **2013**, 13, 3426-3433.

21 Jung, Y.; Shen, J.; Liu, Y.; Woods, J. M.; Sun, Y.; Cha, J. J. Metal Seed Layer Thickness-Induced Transition from Vertical to Horizontal Growth of MoS_2 and WS_2. *Nano Lett.* **2014**, 14, 6842-6849.

22 Wang, H.; Tsai, C.; Kong, D.; Chan, K.; Abild-Pedersen, F.; Nørskov, J. K.; Cui, Y. Transition-Metal Doped Edge Sites in Vertically Aligned MoS_2 Catalysts for Enhanced Hydrogen Evolution. *Nano Res.* **2015**, 8, 566-575.

23 Fei, L.; Lei, S.; Zhang, W.-B.; Lu, W.; Lin, Z.; Lam, C. H.; Chai, Y.; Wang, Y. Direct TEM Observations of Growth Mechanisms of Two-Dimensional MoS_2 Flakes. *Nat. Commun.* **2016**, 7, 12206.

24 Deng, Z. H.; Li, L.; Ding, W.; Xiong, K.; Wei, Z. D. Synthesized Ultrathin MoS_2 Nanosheets Perpendicular to Graphene for Catalysis of Hydrogen Evolution Reaction. *ChemComm* **2015**, 51, 1893-1896.

25 Lan, F.; Lai, Z:; Xu, Y.; Cheng, H.; Wang, Z.; Qi, C.; Chen, J.; Zhang, S. Synthesis of Vertically Standing MoS_2 Triangles on SiC. *Sci. Rep.* **2016**, 6, 31980.

26 Li, S.; Wang, S.; Salamone, M. M.; Robertson, A. W.; Nayak, S.; Kim, H.; Tsang, S. C. E.; Pasta, M.; Warner, J. H. Edge-Enriched 2D MoS_2 Thin Films Grown by Chemical Vapor Deposition for Enhanced Catalytic Performance. *ACS Catal.* **2017**, 7, 877-886.

27 Arrouvel, C.; Breysse, M.; Toulhoat, H.; Raybaud, P. A Density Functional Theory Comparison of Anatase (TiO_2)- and γ-Al_2O_3-Supported MoS_2 Catalysts. *J. Catal.* **2005**, 232, 161-178.

28 Costa, D.; Arrouvel, C.; Breysse, M.; Toulhoat, H.; Raybaud, P. Edge Wetting Effects of γ-Al_2O_3 and Anatase-TiO_2 Supports by MoS_2 and CoMoS Active Phases: A DFT Study. *J. Catal.* **2007**, 246, 325-343.

29 Helveg, S. An Industrial Perspective of the Impact of Haldor Topsøe on (*In Situ*) Electron Microscopy in Catalysis. *J. Catal.* **2015**, 328, 102-110.

30 Tao, F.; Crozier, P. A. Atomic-Scale Observations of Catalyst Structures under Reaction Conditions and during Catalysis. *Chem. Rev.* **2016**, 116, 3487-3539.

31 Ross, F. M. Opportunities and Challenges in Liquid Cell Electron Microscopy. *Science* **2015**, 350, aaa9886.

32 Feldman, Y.; Wasserman, E.; Srolovitz, D. J.; Tenne, R. High-Rate, Gas-Phase Growth of MoS_2 Nested Inorganic Fullerenes and Nanotubes. *Science* **1995**, 267, 222-225.

33 Feldman, Y.; Frey, G. L.; Homyonfer, M.; Lyakhovitskaya, V.; Margulis, L.; Cohen, H.; Hodes, G.; Hutchison, J. L.; Tenne, R. Bulk Synthesis of Inorganic Fullerene-Like MS2 (M = Mo, W) from the Respective Trioxides and the Reaction Mechanism. *J. Am. Chem. Soc.* **1996**, 118, 5362–5367.

34 Brandt, B. G.; Skapski, A. C. A Refinement of the Crystal Structure of Molybdenum Dioxide. *Acta Chem. Scand.* **1967**, 21, 661-672.

35 Wienold, J.; Jentoft, R. E.; Ressler, T. Structural Investigation of the Thermal Decomposition of Ammonium Heptamolybdate by I*n Situ* XAFS and XRD. *Eur. J. Inorg. Chem.* **2003**, 2003, 1058-1071.

36 Stockmann, R. M.; Zandbergen, H. V.; Langeveld, A. D. v.; Moulijn, J. A. Investigation of MoS_2 on γ-Al_2O_3 by HREM with Atomic Resolution. *J. Mol. Catal. A: Chem.* **1995**, 102, 147–161.

37 Hansen, L. P.; Johnson, E.; Brorson, M.; Helveg, S. Growth Mechanism for Single- and Multi-Layer MoS_2 Nanocrystals. *J. Phys. Chem. C* **2014**, 118, 22768-22773.

38 Margulis, L.; Salitra, G.; Tenne, R.; Talianker, M. Nested Fullerene-Like Structures. *Nature* **1993**, 365, 113-114.

39 Shannon, R. D.; Rossi, R. C. Definition of Topotaxy. *Nature* **1964**, 202, 1000-1001.

40 Muijsers, J. C.; Weber, T.; Vanhardeveld, R. M.; Zandbergen, H. W.; Niemantsverdriet, J. W. Sulfidation Study of Molybdenum Oxide Using $MoO_3/SiO_2/Si(100)$ Model Catalysts and Mo-$^{IV}{}_3$-Sulfur Cluster Compounds. *J. Catal.* **1995**, 157, 698-705.

41 Weber, T.; Muijsers, J. C.; van Wolput, J. H. M. C. ; Verhagen, C. P. J.; Niemantsverdriet, J. W. Basic Reaction Steps in the Sulfidation of Crystalline MoO_3 to MoS_2, As Studied by X-ray Photoelectron and Infrared Emission Spectroscopy. *J. Phys. Chem.* **1996**, 100, 14144–14150.

42 Tauster, S. J.; Pecoraro, T. A.; Chianelli, R. R. Structure and Properties of Molybdenum Sulfide: Correlation of O_2 Chemisorption with Hydrodesulfurization Activity, *J. Catal.* **1980**, 63, 515-519.

43 Shi, Q.; Li, Y.; Zhou, Y.; Miao, S.; Ta, N.; Zhan, E.; Liu, J.; Shen, W. The Shape Effect of TiO_2 in Vox/TiO_2 Catalysts for Selective Reduction of NO by NH_3. *J. Mater. Chem. A* **2015**, 27, 14409-14415.

44 Picher, M.; Mazzucco, S.; Blankenship, S.; Sharma, R. Vibrational and Optical Spectroscopies Integrated with Environmental Transmission Electron Microscopy. *Ultramicroscopy* **2015**, 150, 10-15.

45 Mele, L.; Konings, S.; Dona, P.; Evertz, F.; Mitterbauer, C.; Faber, P.; Schampers, R.; Jinschek, J. R. MEMS-Based Heating Holder for the Direct Imaging of Simultaneous *In Situ* Heating and Biasing Experiments in Scanning/Transmission Electron Microscopes. *Microsc. Res. Tech.* **2016**, 79, 239-250.

46 Hansen, P. L.; Helveg, S.; Datye, A. K. Atomic-Scale Imaging of Supported Metal Nanocluster Catalysts in the Working State. *Adv. Catal.* **2006**, 50, 77-95.

47 Allard, L. F.; Bigelow, W. C.; Jose-Yacaman, M.; Nackashi, D. P.; Damiano, J.; Mick, S. E. New MEMS-Based System for Ultra-High-Resolution Imaging at Elevated Temperatures. *Microsc. Res. Tech.* **2009**, 79, 208-215.

48 Helveg, S.; Kisielowski, C. F.; Jinschek, J. R.; Specht, P.; Yuan, G:; Frei, H. Observing Gas-Catalyst Dynamics at Atomic Resolution and Single-Atom Sensitivity. *Micron* **2015**, 68, 176-185.

49 Kilaas, R. *Total Resolution LLC: Software for High Resolution Electron Microscopy*, <http://www.totalresolution.com> (2016).

50 Mortensen, J. J.; Hansen, L. B.; Jacobsen, K. W. Real-Space Grid Implementation of the Projector Augmented Wave Method. *Phys. Rev. B* **2005**, 71, 035109.

51 Enkovaara, J.; Rostgaard, C; Mortensen, J. J.; Chen, J.; Dulak, M.; Ferrighi, L.; Gavnholt, J; Glinsvad, C; Haikola, V.; Hansen, H. A. *et al*. Electronic Structure Calculations with GPAW: A Real-Space Implementation of the Projector Augmented-Wave Method. *J. Phys.: Condens. Matter* **2010**, 22, 253202.

52 Bahn, S. R.; Jacobsen, K. W. An Object-Oriented Scripting Interface to a Legacy Electronic Structure Code. *Comput. Sci. Eng.* **2002**, 4, 56-66.

53 Chase, M. W. *NIST-JANAF Thermochemical Tables*. 4 edn, (American Chemical Society, 1998).

Figure 1. Surface sulfidation of MoO_2 nanocrystals. **a** An illustration of a MoO_2 nanocrystal before and after partial sulfidation by heating in H_2S/H_2. In the sulfided state, a partial coverage of co-existing *e*-MoS_2 and *p*-MoS_2 phases is illustrated by the MoS_2 sheets (yellow) orientated perpendicular to and along the MoO_2 crystal facets (blue), respectively. **b, c** TEM images of MoO_2 nanocrystals after exposure to 10% H_2S in H_2 *in situ* at (b) 250°C for 300 min and (c) 300°C for 240 min. The images are acquired in the microscope base vacuum ($5*10^{-6}$ mbar) at 120°C. A distinct lattice constant with the MoS_2 (002) lattice spacing of 0.62nm and the MoS_2 (100) lattice spacing of 0.27 nm are resolved at the surface of the MoO_2 nanocrystals in b and c. Crystal lattice planes with spacing corresponding to MoO_2 are resolved in the bulk of the nanoparticles.

Figure 2. Time-resolved TEM imaging of a MoO_2 nanocrystal *in situ* during sulfidation. **a-f** Time-resolved TEM of a MoO_2 nanocrystal during the exposure to 1 mbar of 10% H_2S in H_2 at 250°C. The images are extracted from Video S1 in the Supporting Information at times [and accumulated electron dose] of (a) 45 min [9×10^3 $e^-/Å^2$], (b) 65 min [27×10^3 $e^-/Å^2$], (c) 85 min [45×10^3 $e^-/Å^2$], (d) 160 min [81×10^3 $e^-/Å^2$], (e) 220 min [126×10^3 $e^-/Å^2$] and (f) 280 min [153×10^3 $e^-/Å^2$]. The time of 0 min corresponds to the time of gas introduction in the experiment. The inserts show Fast Fourier Transforms of the corresponding images. The open arrowhead indicates the location of *e*-MoS_2. First the MoO_2 (01-1) and later the (20-2) lattice planes are visible in the MoO_2 bulk due to slight rotation of the nanocrystal with time. All TEM images have the same size.

Figure 3. Interface between *e*-MoS_2 and MoO_2**. a** Close-up high resolution TEM image of the nanocrystal in Figure 2, acquired *post mortem* after sulfidation for 300 min exposure to 1 mbar 10% H_2S in H_2 at 250°C. The superimposed crystal lattice vectors and zone axis (Z.A.) correspond to MoO_2. **b** FFT image revealing the MoO_2 (20-2), MoO_2 (11-1) and MoS_2 (002) lattice planes, corresponding to a zone axis (Z.A.) view of the MoO_2 nanocrystal in the [101] direction. **c** Image intensity line-scans in MoO_2 and *e*-MoS_2 obtained along MoO_2[20-2] and averaged over 10 pixels corresponding to the blue (MoO_2), orange (*e*-MoS_2) and yellow (*e*-MoS_2) boxes in (a).

Figure 4. Atomic mechanism for topotaxy of *e*-MoS_2 at the MoO_2(110) surface. **a-d** The topotactic transformation is illustrated by ball models of the atomic structures at an inclined projection (left) and by sketches of the [-11-1] oriented atomic rows with Mo in the center and the anionic content as the rim (right). The colors coding is dark blue for Mo in [-11-1] rows with the bulk density (full row), light blue for Mo in [-11-1] rows with half the bulk density (half row), red for O and yellow for S. Crystal directions are quoted with reference to the MoO_2 lattice. The atomic row numbering is equivalent in the ball models and sketches. All surface structures are obtained by DFT calculations. **a** Initial state for the sulfided MoO_2(110) surface (indicated by the dashed line). **b** The sulfided MoO_2(110) surface after displacement of row 1. **c** The sulfided MoO_2(110) surface in (b) after displacement of row 3 and surface O-S exchange of the exposed oxide surface in rows 2, 4 and 5, resulting in a two-row *e*-MoS_2 sheet. **d** The sulfided MoO_2(110) surface in (c) after displacement row 4 and 5 and O-S exchange in the

exposed oxide surface, resulting in a four-row *e*-MoS_2 sheet aligned with the MoO_2(20-2) planes. **e** Calculated Gibbs free energies per unit cell for (a-d) for both the MoO_2(110) and (010) surfaces (Methods).

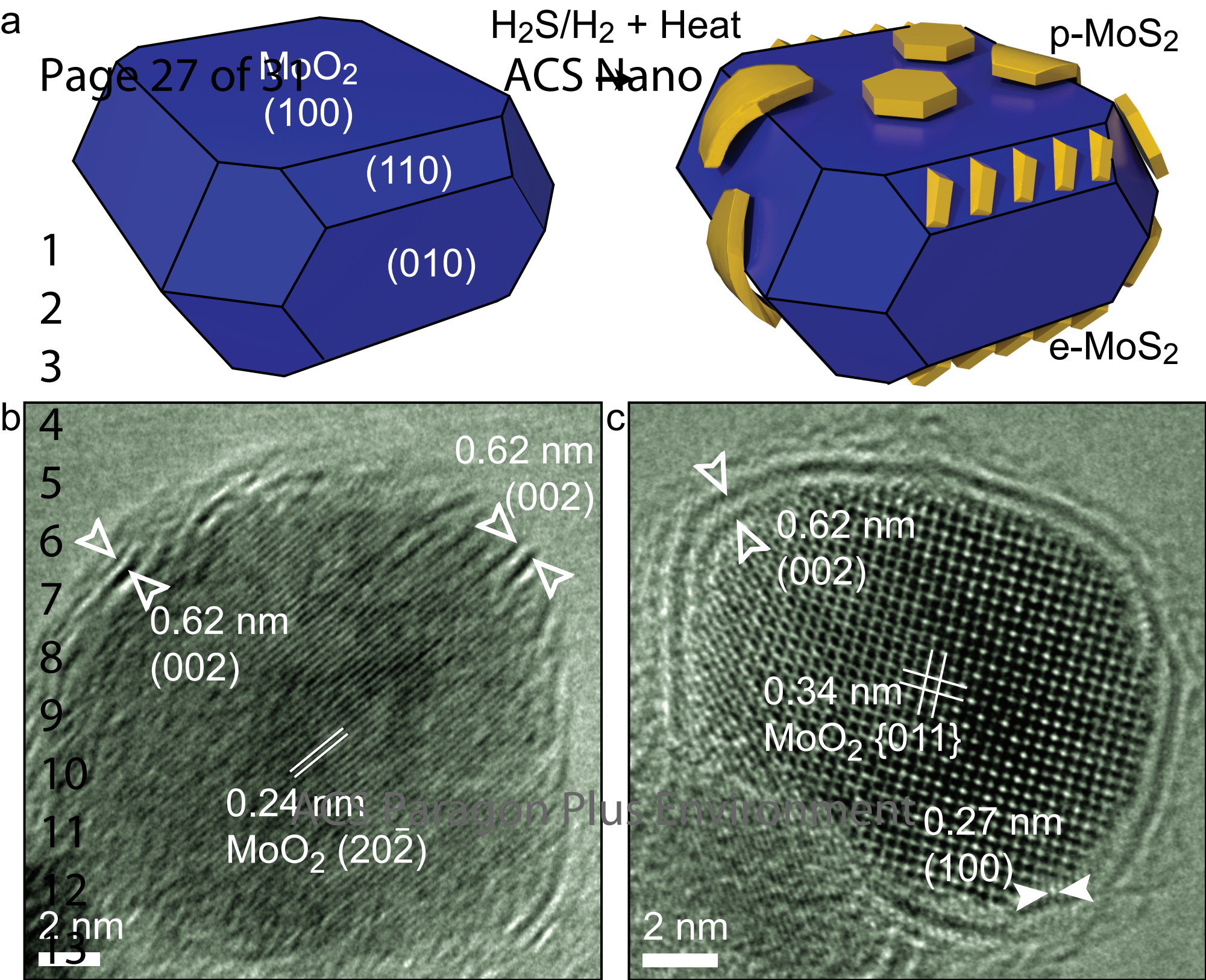

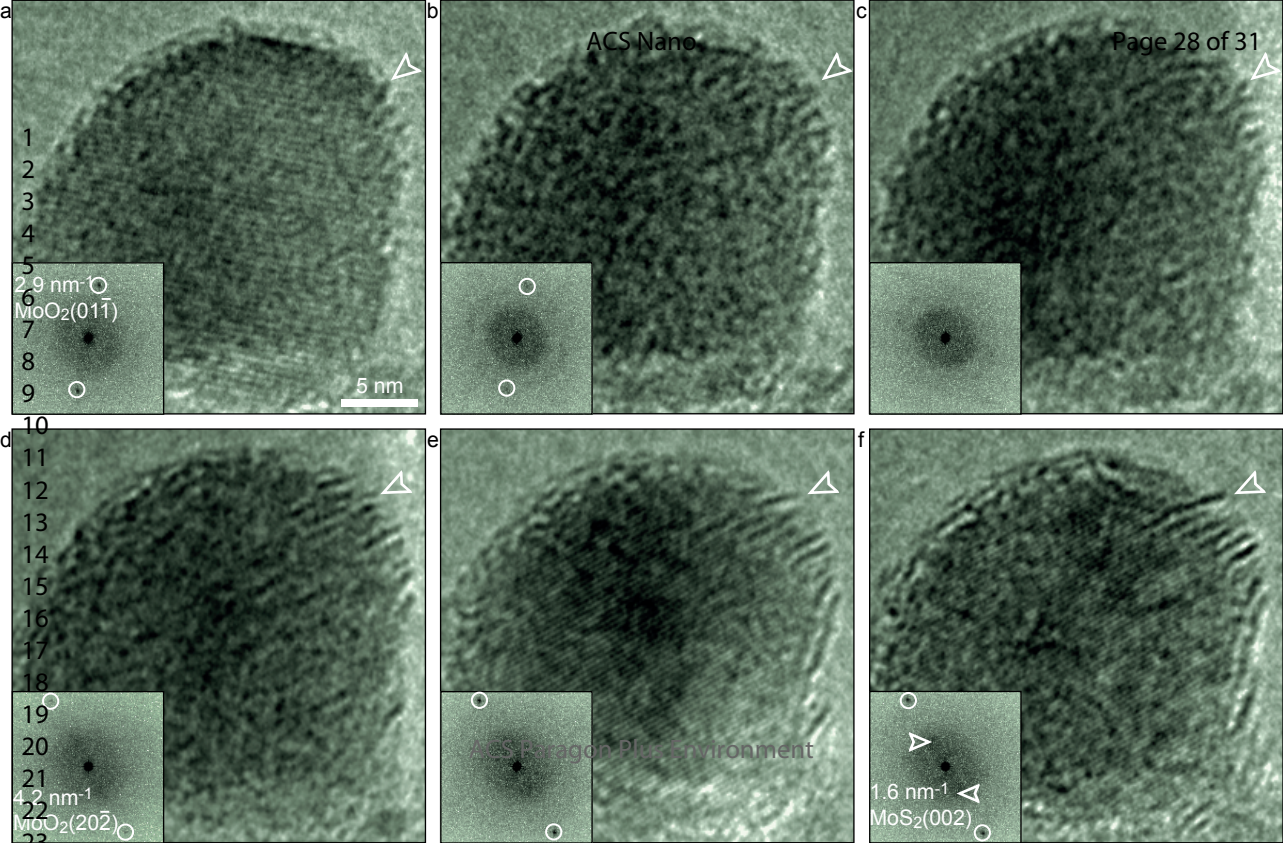

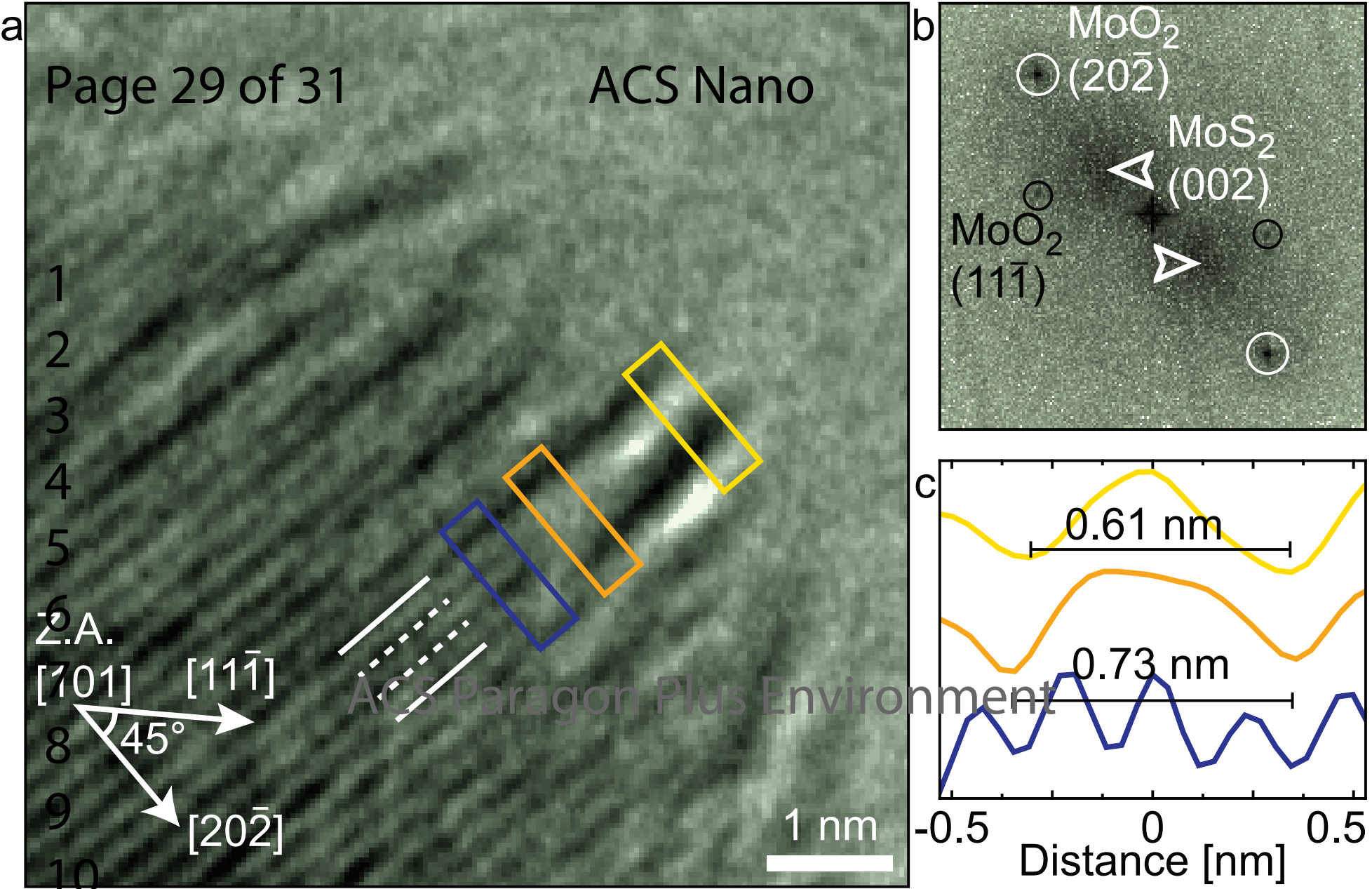

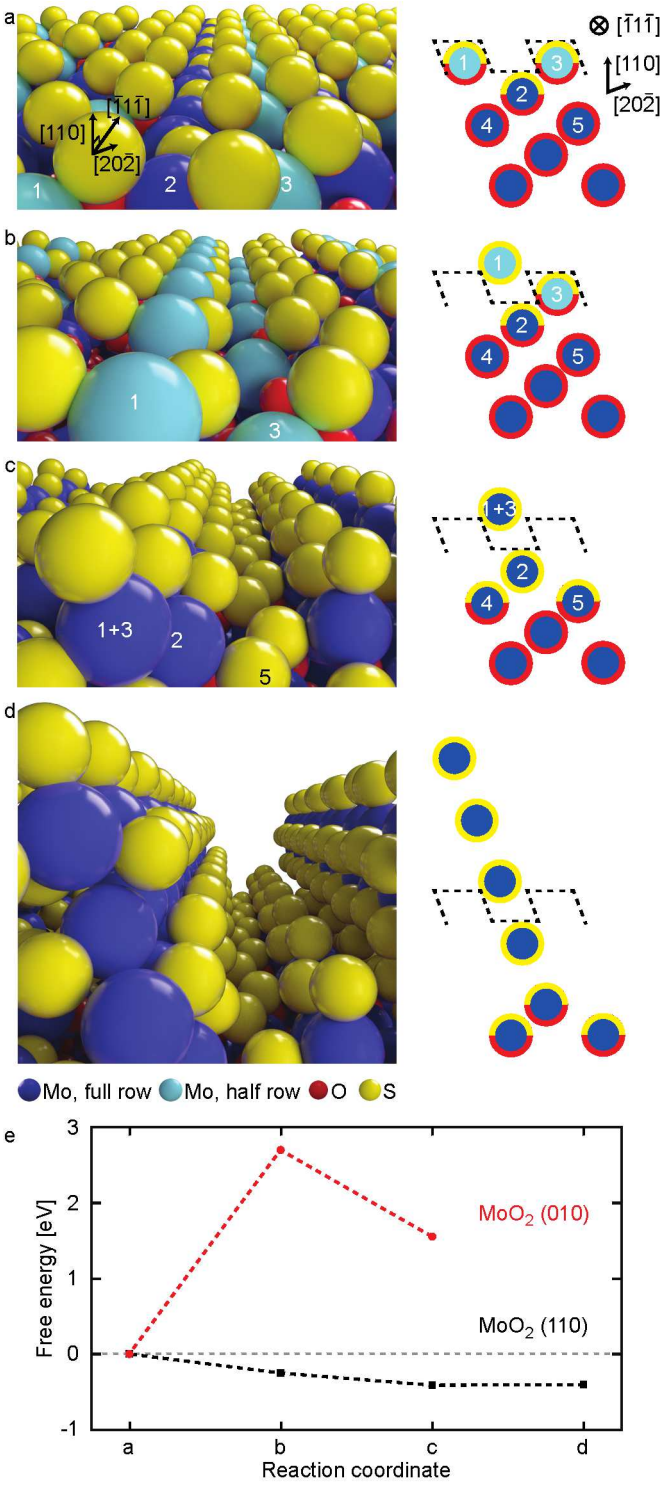
a
b
c
d
[1̄1̄1̄]
[110]
[20̄2̄]
1
2
3
4
5
1+3
Mo, full row
Mo, half row
O
S
e
Free energy [eV]
MoO2 (010)
MoO2 (110)
Reaction coordinate

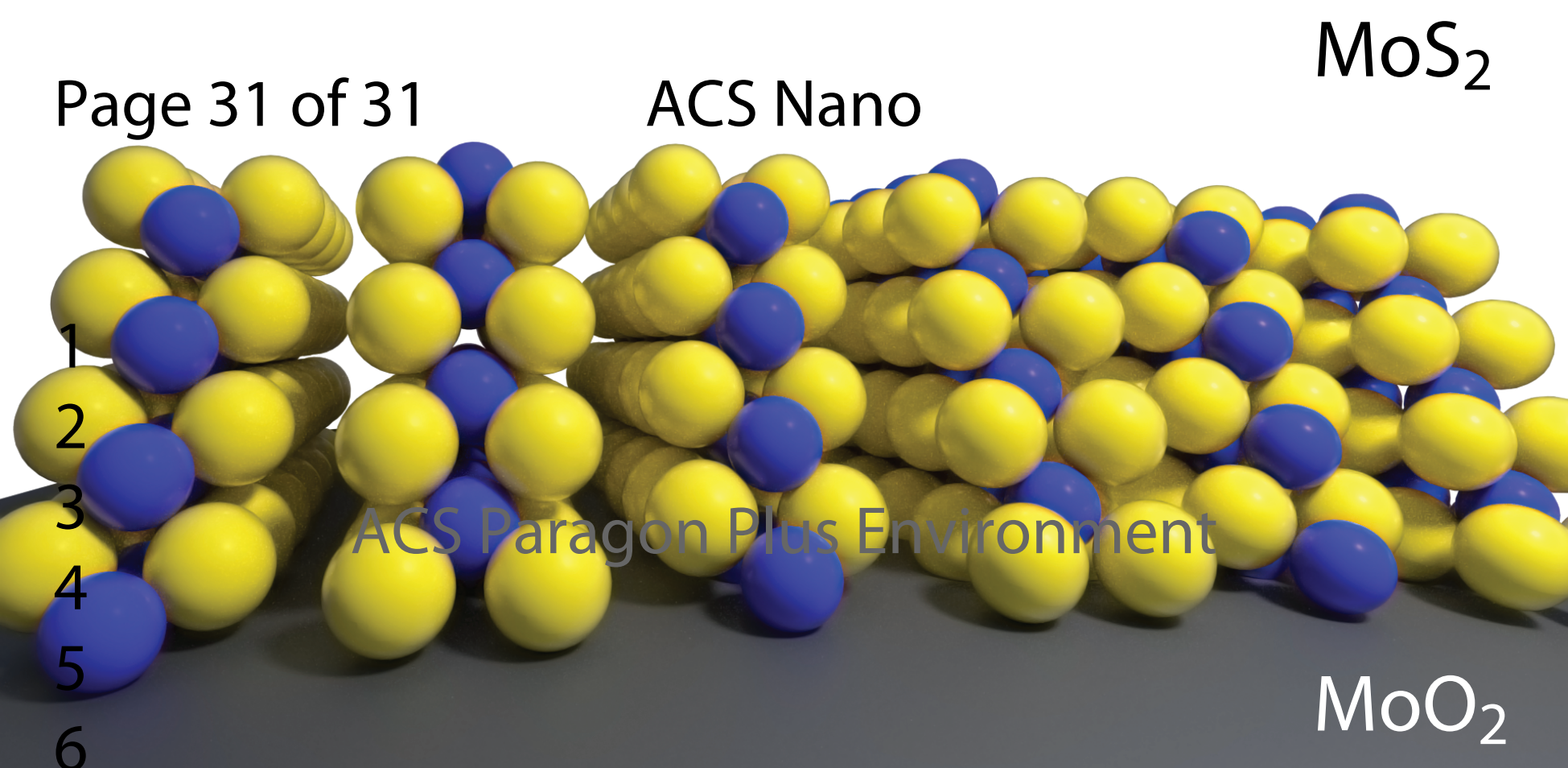
MoS_2
1
2
3
4
5
6
ACS Paragon Plus Environment
MoO_2